PCCP

Ultra-fast Excited-state Dynamics of Substituted trans-Naphthalene Azo Moieties

Journal:	*Physical Chemistry Chemical Physics*
Manuscript ID	CP-ART-03-2023-001211.R1
Article Type:	Paper
Date Submitted by the Author:	02-May-2023
Complete List of Authors:	Hamburger, Robert C; Lehigh University Huang, Tao; Lehigh University, Department of Chemisry Martin, Shea; Lehigh University, Department of Chemisry Pointer, Craig; Lehigh University, Department of Chemisry Fredin, Lisa; Lehigh University, Lisa Fredin; Young, Elizabeth; Lehigh University, Department of Chemistry

ARTICLE

Ultra-fast Excited-state Dynamics of Substituted *trans*-Naphthalene Azo Moieties

Received 00th January 20xx,
Accepted 00th January 20xx

DOI: 10.1039/x0xx00000x

Robert C. Hamburger, [a] Tao Huang, [a] Shea M. Martin, [a] Craig A. Pointer, [a] Lisa A. Fredin*[a] and Elizabeth R. Young*[a]

In this work we untangle the ultrafast deactivation of high energy excited states in four naphthalene-based azo dyes. Through systematic photophysical and computational study, we observed a structure-property relationship in which increasing the electron donating strength of the substituent leads to longer lived excited states in these organic dyes and faster thermal reversion from the *cis* to *trans* configuration. In particular, azo dyes **1** – **3** containing less electron donating substituents show three distinct excited-state lifetimes of ~ 0.7–1.5ps, ~ 3–4 ps, and 20–40 ps whereas the most electron donating dimethyl amino substituted azo **4** shows excited-state lifetimes of 0.7 ps, 4.8 ps, 17.8 ps and 40 ps. While bulk photoisomerization of all four moieties is rapid, the *cis* to *trans* reversion lifetimes vary by a factor of 30 with $\tau_{reversion}$ decreasing from 276 min to 8 min with increasing electron donating strength of the substituent. In order to rationalize this change in photophysical behavior, we explored the excited-state potential energy surfaces and spin-orbit coupling constants for azo **1** – **4** through density functional theory. The increase in excited-state lifetime for **4** can be attributed to geometric and electronic degrees of freedom of the lowest energy singlet excited state potential energy surface.

Introduction

Azo dyes are the single most commonly utilized dyes used in industrial processes,[1] found in everything from food colorants and cosmetic additives[2] to textile reagents,[3] biologic indicators,[4] and organic synthons.[5] In addition, their light-driven reactivities such as the *trans*/*cis* isomerization and proton-transfer induced tautomerization have made them good candidates in the applications of functional materials, electronic devices and drug delivery.[6–10] Recently, our group has reported that anthracene-based azo dyes may potentially be employed in light-induced proton-coupled electron transfer reaction (PCET),[11,12] which is a fundamental pathway used in the renewable energy generation.[13] Naphthalene-derived azo molecules are also interesting as they are structural analogs of well-studied azobenzenes[14–16] and our previously reported anthracene azo species.[11,12] In order for azo molecules to be employed successfully in various applications, a thorough understanding of their electronic properties and excited-state dynamics is necessary. Towards this goal, this work focuses on understanding the detailed excited-state dynamics of a series of naphthalene-based azo dyes (Scheme 1) using ultra-fast time-resolved spectroscopy and quantum mechanics calculations.

Scheme 1. Derivatized naphthalene-based azo dyes

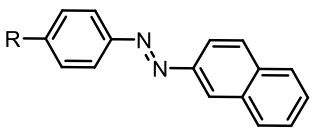

1. R = H; **2.** R = OH
3. R = OMe; **4.** R = NMe_2

Excited-state evolution including photoisomerization has been studied extensively in azobenzene following excitation into either the nπ* or ππ* states. Mechanistic proposals have described photoisomerization via torsional rotation of the ∠CNNC dihedral angle,[17,18] inversion of ∠CNN angle,[17] or a combined, concerted pathway.[19,20] While mechanisms in symmetric azobenzene have been investigated,[6] the effects of substitutions and asymmetry around the azo bond need to be more fully explored. Fortunately, azo dyes possess great synthetic accessibility that imparts tunability of the electronic structure through simple functionalization and that can provide important insights into structure-property relationships of azo dyes.

[a] *Department of Chemistry, Lehigh University, 6 E. Packer Ave., Bethlehem, PA 18015, USA.*

Electronic Supplementary Information (ESI) available Synthetic details, ^{1}H NMR spectra, photoisomerization and reversion data, molar absorbtivities of **1**-**4**, transient absorption fitting analysis, DFT computed molecular orbital diagrams, relevant geometries of singlets, triplets and transitions states, potential energy surface, TDDFT energy tables, spin-orbit coupling constants. See DOI: 10.1039/x0xx00000x

Relatively few studies have delved into the ultrafast dynamics of these azo moieties to establish how synthetic alteration impacts the photophysics of their deactivation. Wachtveitl investigated the ultrafast dynamics of bisazobenzenes that were connected via the *ortho-*, *meta-*, and *para-* positions of the adjoining benzene group. They reported that the functionalization position on the benzene dramatically impacted the quantum yields of isomerization and the *cis* to *trans* thermal reversion lifetimes.[21] Elles and Ramamurthy reported the ultrafast dynamics of azobenzene substituted at the 4-position by methyl, ethyl or propyl groups and the impact of confinement on the isomerization dynamics, showing that encapsulation increases the excited-state lifetimes and alters the yields of the *trans* to *cis* photoisomerization reaction compared with the dyes in solution.[22,23] Following $\pi\pi^*$ excitation, the crowded environment of the confined system that resulted from the lengthening of the alkyl tails resulted in deeper trapping of the excited-state species. Additional azobenzene derivatives have been examined in the liquid crystal phase, which shifts the potential energy difference between $n\pi^*$ and $\pi\pi^*$ states.[24,25] Finally, other photoswitches have been examined for the effects of substituent character on photoswitching speed and mechanism.[26]

While the naphthalene-azo-benzene motif has been employed in a wide scope of commercially available azo dyes, their excited-state properties still remain unillustrated. This systematic study focuses on the photophysical properties of naphthalene-based azo dyes containing electron-donating groups appended to the phenyl side of an azo bond. The results provide important insights into multipath deactivation of excited states in this organic system. In addition, the asymmetric nature of the dyes – with naphthalene on one side of the azo bond and phenyl on the opposite side – provides a means to explore how asymmetry impacts the isomerization and reversion mechanisms.

Experimental

All reagents were obtained from commercial sources used as received without further purification, unless otherwise specified. Air-sensitive reactions were conducted using a standard Schlenk line techniques under nitrogen. Acetonitrile was dried over CaH_2 and distilled. Dried acetonitrile was stored over 4 Å sieves.

Instrumentation. The ^1H spectra were recorded on a Bruker 400 MHz or 500 MHz spectrometer and were calibrated to the residual solvent signals. Chemical shifts are reported in parts per million (ppm). Signal multiplicities are abbreviated as: s (singlet), d (doublet), t (triplet), m (multiplet). Molar absorptivity was acquired with Cary 5000 UV-vis-NIR spectrometer. Photoisomerization data were acquired using an Ocean Optics Flame UV-vis diode array. Fluorescence spectra were acquired with a BH Chronos steady-state fluorimeter.

Synthesis. All synthetic protocols and NMR (including peak assignments) of **1 – 4** are reported in the Supporting Information.

Transient Absorption Spectroscopy. Femtosecond transient absorption spectroscopy was performed with an Ultrafast Systems Helios spectrometer. One hundred fifty femtosecond pulses of 800 nm laser light were generated with a Coherent Libra amplified Ti:sapphire system at 1.2 W and 1 kHz repetition rate. A beam splitter is used to send approximately 80% of the 800 nm pulses to a Topas-C optical parametric amplifier to generate a 370 nm pump pulse. The pump pulse was attenuated to between 0.1 mW and 0.4 mW to prevent decomposition of the sample. The remainder each pulse (~20% of the 800 nm light) was sent through a CaF_2 crystal to generate a white light continuum for use as the probe pulse. The probe pulse traveled along a delay stage to generate the pump-probe time delay and a chopper was used to remove every other pump pulse. For each time delay, a series of unpumped and pumped probe pulses were recorded. In each case, a reference probe pulse (that does not go through the sample) was collected and processed to improve the S/N while minimizing the number of scans needed to obtain quality data. The transient absorption spectra were measured over a 5 ns window. For each scan, 250 time points were recorded with exponentially spaced time points and each sample was subjected to three scans. The sample was stirred with a magnetic stir bar during every run.

Scheme 2. Synthesis of azo dyes **1** – **4**.

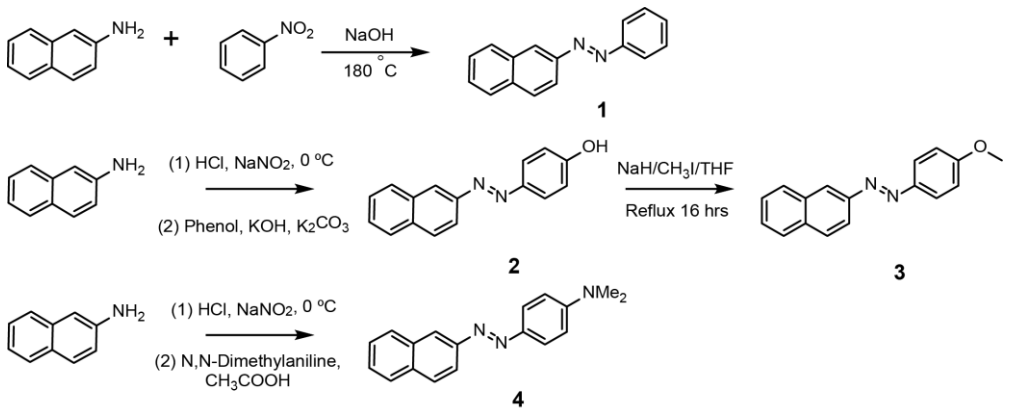

Samples for transient absorption spectroscopy were prepared in on high vacuum line in a 2-mm quartz high-vacuum cuvette. The concentration of each dyad was 30 µM. UV-visible absorption spectra were recorded before and after each TA experiment to verify that no decomposition had occurred. A chirp correction was applied prior to analysis of each data set. Data analysis was performed using the global analysis software Surface Xplorer provided free of charge by Ultrafastsystems. Fitting was done by extracting and retaining as many principal components as necessary to approximate the data surface (approximately 10 PC or more). Principal component kinetic traces were then fit and decay-associated difference spectra (DADS) and their corresponding lifetimes were generated. The extracted modeled lifetimes and DADS were then used to re-construct a fit surface that was compared with the original data set. Quality of the fitting was assessed by subtracting the fit surface from the original data surface generating a residual surface. Each residual was also assessed with a residual standard error in order to facilitate comparison between fit models.

Fluorescence Quantum Yields. All samples were prepared in acetonitrile to have less than 0.1 AU absorbance at the excitation wavelength in order to minimize the internal filter effect. Each sample was freeze-pump-thawed on a high-vacuum line to degas the samples (mTorr pressure in the cuvette). Samples were excited at 300 nm and emission was monitored from 320 nm to 600 nm. 1,4-Bis(5-phenyloxazol-2-yl)benzene (POPOP) was used as a quantum yield standard (QY = 0.97)[27]. Azobenzene was also used for its spectral similarity to the naphthalene-based azo-dye samples. POPOP and azobenzene (QY = 2.53 × 10^{-5})[14] were used as standards to experimentally measure the QY and verify the accuracy of our set up. We verified our setup and reproduced QY values of 1.03 and 3.68 × 10^{-5} for POPOP and azobenzene respectively, in line with literature values. Sample absorbance and emission of **1 – 4** were measured in triplicate and their quantum yields were calculated using the following equation,

$$\phi_r = \phi_s \times \frac{I_r\, A_s}{I_s\, A_r} \times \frac{\eta_r}{\eta_s}$$

where $\boldsymbol{\varphi}$ is the fluorescence quantum yield, ***I*** represents the integrated fluorescence intensity of emitted light, ***A*** is the absorbance of the sample at the excitation wavelength, $\boldsymbol{\eta}$ is the refractive index of the solvent used, and ***r*** and ***s*** represent the unknown and standard samples respectively.

Photoisomerization. Samples of **1 – 4** were prepared in dry acetonitrile to an absorbance of ~1 AU at the absorption maximum (~ 0.1 mM). Each sample was freeze-pump-thawed on a high-vacuum line to degas the samples to ~mTorr pressure in the cuvette. *To measure the trans → cis conversion*: The absorbance of each sample was measured at set intervals using an Ocean Insight diode array spectrometer to capture the entire spectrum in a 1.25 second acquisition. Samples of **1 – 3** were illuminated using a UV LED (λ_{max} = 370 nm, whm = 12 nm) using an LEDi-UV photolysis lamp head and a Luzchem LED Illuminator with constant illumination at 155 mW. Samples of **4** were illuminated with a blue LED (λ_{max} = 453 nm, whm = 18 nm) using an LEDi-RGB photolysis lamp head and a Luzchem LED Illuminator with constant illumination at 120 mW. Spectra were measured every 1.25 seconds during the course of the illumination until spectrum stopped changing (indicating conversion to *cis* configuration). At this point the conversion reaction was considered complete. *To measure the cis → trans conversion*: The absorption of the final "conversion reaction" product was measured with the laser shining on the sample. As the illumination was shut off, the absorption spectra collection was initiated. The reversion reaction was carried out with no illumination enclosed in the sample holder under ambient condition. Spectra were measured every 1.25 seconds with

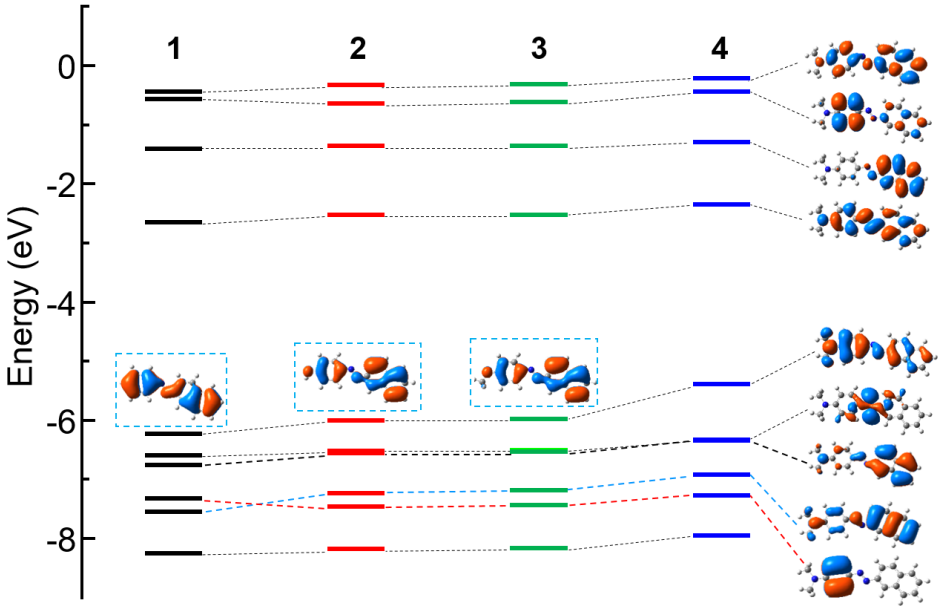

Figure 1. Frontier molecular of azo **1** – **4**. B3LYP/6-311G(d,p)/PCM(ACN). All orbitals shown in Figures S6-S9.

scans being retained periodically based on the rate of the reversion reaction until the initial *trans* configuration spectrum was obtained or the spectrum remained constant.

Quantum Mechanical Calculations. Density functional theory (DFT) and time-dependent density functional theory (TDDFT) calculations were performed on representative azo **1** - **4**. The B3LYP functional[28–31] and 6-311G basis set[32–36] were used. An acetonitrile solvent environment was simulated with the polarizable continuum model.[37] All calculations were performed using Gaussian09.[38] All structures were confirmed as local minima or transition states via frequency calculations, with zero and one imaginary frequency, respectively.

Results and discussion

Ground-state characterization. The syntheses of azo **1** – **4** were modified from literature (Scheme 2). Briefly, 2-aminonaphthalene was either condensed with nitrobenzene in melt sodium hydroxide to generate non-substituted azo **1**,[39] or reduced to form diazonium salt by sodium nitrate and further converted to corresponding 4-substituted azo **2** and azo **4**.[12,40] The azo **3** was obtained by the methylating azo **2** in the presence of sodium hydride and iodomethane. The structures were confirmed with ^{1}H NMR reported in the Supporting Information.

The addition of a range of electron donating groups provides a handle to tune the electronic structure of the ground state and the excited-state dynamics of azo **1** – **4**. The density functional theory (DFT) optimized ground-state geometries of azo **1** – **4** show key structural parameters consistent with prior analogues (Figure S48). The frontier molecular orbitals (Figure 1) are similar in both energy and nature when varying the substituents on the phenyl side. The occupied MO energies are more strongly impacted by the substitution. In particular, the highest occupied molecular orbital (HOMO) delocalizes relatively evenly on both phenyl and naphthalene rings and is thus destabilized when the para phenyl position is substituted with an electron-donating group, leading to slight narrowing of the band gap from 3.58 eV to 3.04 eV (Δ = 0.54 eV) going from azo **1** to azo **4**. The non-bonding orbital localized on the azo bond is the HOMO-1 for each molecule. The symmetry of the conjugated π-network (HOMO-2 through HOMO-5) is affected by the electron donations on the phenyl side, leading to slight differences in energy ordering and symmetries of these π-bonding orbitals.

Azo-dyes **1** – **3** show similar absorption spectra (Figure 2) with absorption maxima between 330 – 350 nm and small shoulder peaks at ~ 450 nm (

Table 1). In contrast, azo-dye **4** is significantly red-shifted (by ~80 nm or ~0.6 eV) compared to azo **3**, the most red-shifted of the azo **1** – **3** group. Azo-dye **4** shows with a broad absorption feature centered at ~420 nm and no small shoulder peaks akin to the ones observed in **1** – **3**.

Time-dependent DFT (TDDFT) transitions capture the major absorption features (Figure 3, Tables S1, 3, 5, 7) for each azo-

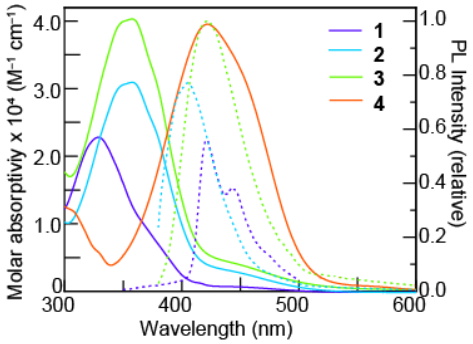

Figure 2. Electronic absorption spectra (solid lines) and steady photoluminescence spectra (dotted lines) of azo **1**-**4** in acetonitrile. The photoluminescence of azo **1**-**3** were collected with λ_{ex} = 330 nm, 355 nm, and 355 nm, respectively. The emission spectrum of azo **4** was not detected and is therefore absent in the figure.

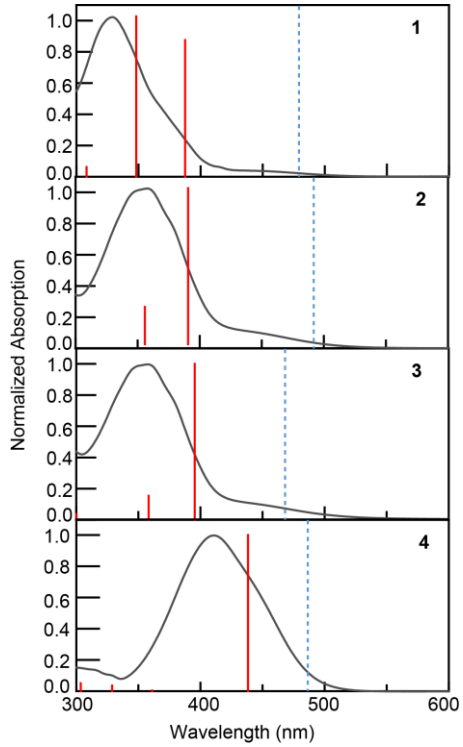

Figure 3. B3LYP/6-311G(d,p)/PCM(ACN) predicted transitions (red) for azo **1** – **4** under the experimental absorption spectra (black). The lowest-energy symmetry-forbidden transitions (S_1, n → π*) are thus shown as a blue dot line as their computed oscillator strength is zero.

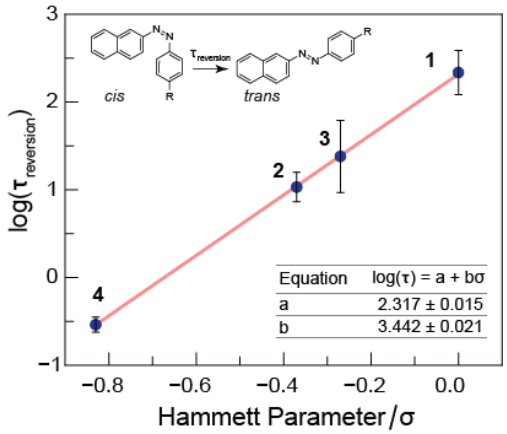

Figure 4. Plot of log($\tau_{reversion}$) for *cis* → *trans* thermal reversion lifetime as a function of Hammett parameter.

dye. For azo **1 – 3**, the major absorption peak is $\pi \rightarrow \pi^*$, calculated as the S_2 (HOMO → LUMO) and S_3 (HOMO-2 → LUMO) transitions (Table S1, S3, and S5). The S_1 in each azo-dye is a symmetry forbidden $n \rightarrow \pi^*$ transition (computed oscillator strength zero) and is shown in Figure 3 as a dotted, blue stick to differentiate it from the predicted allowed transitions. In fact, the small shoulder peaks observed at ~450 nm are likely this lowest-energy $n \rightarrow \pi^*$ symmetry forbidden transition (S_1), which occur in solution due to vibrational and torsional degrees of freedom breaking the molecular symmetry. For azo **4**, the predicted S_2 excitation is significantly red shifted as compared to the S_2 states of azo **1 – 3** due to the decrease of the band gap driven by destabilization of the HOMO (*vide supra*). Additionally, due to the virtually isoenergetic HOMO-1 (n orbital) and HOMO-2 (π orbital), the S_3 transition in **4** has significant mixing between the HOMO-2 → LUMO and HOMO-1 → LUMO (unallowed $n \rightarrow \pi^*$) that results in no appreciable oscillator strength. Accordingly, only one predicted transition corresponding to the S_2 state of **4** is found within the lowest-energy absorption peak centered at ~400 nm.

Photoluminescence. When excited at the main visible absorption peak of each dye, weak emission is observed at 421 nm, 403 nm and 420 nm for azo **1 – 3**, respectively (Figure 2). In contrast to azo **1 – 3**, no photoluminescence signal was observed when the main absorption peak of azo **4** was excited (c.a. λ_{ex} = 420 nm).

Although azo molecules are some of the most widely studied organic dyes, in the case of azobenzene, there are only limited reports of the steady-state fluorescence spectrum, due to its very low quantum yield (less than 0.01%).[41] Anthracene-based azo dye analogues possess slightly higher reported quantum yields of (0.33 – 0.55%)[12] more in line with the unambiguous fluorescence observed for azo **1 – 3**. The emission bands of azo **1 – 3** are higher in energy than the lowest-lying, weakly absorbing shoulder peaks in the absorption spectrum (~ 400 – 500 nm). These observations are consistent with prior steady-state fluorescence study of azobenzene[41] that have shown S_2 fluorescence is more intense than S_1 fluorescence due to the optically forbidden nature of S_1 excited state. Therefore, these azo moieties, as others before them, do not obey Kasha's rule.[42–45] Based on TDDFT singlet transitions in azo **1 – 3**, the observed emission would be attributed to a similar $S_2(\pi\pi^*) \rightarrow$ ground state allowed transition at ~ 400 nm, and not the lower energy $S_1(n\pi^*)$ emission at ~ 500 nm, as expected.

Emission quantum yield measurements were carried out in acetonitrile under inert conditions using 1,4-bis(5-phenyloxazol-2-yl)benzene (POPOP) as a quantum yield standard. Samples were excited at 300 nm and emission was monitored from 320 nm to 600 nm. Consistent with previous reports of azobenene derivatives, **1 – 3** exhibit a low quantum yield value of less than 0.1% (

Table 1).

In contrast, excitation of **4** into the main absorption peak (c.a. λ_{ex} = 420 nm) leads no emission. By perturbing the electronics of the system with addition of the most electron donating (dimethylamine) substituent, population of S_3 from ground state excitation is forbidden, *vide supra*, in contrast to azo **1 – 3** (in which population of both S_2 and S_3 are allowed). Therefore, when **4** is excited at 420 nm, population of the S_2 state dominates leading to an exclusively non-radiative pathway, likely dominated by vibrational relaxation that leads to no measurable emission.

Photoisomerization and reversion. Each azo derivative (**1 – 4**) undergoes rapid bulk *trans* → *cis* isomerization upon steady-state excitation with a photolysis lamp (Figure S1). When the

Table 1. Photophysical Data and Excited-State Lifetimes Recorded of Azo **1**-**4**

	Abs λ_{max} (nm)	**PL λ_{max}** (nm)	**PL QY** (%)	τ_1 (ps) $^*S_1 \rightarrow S_1$	τ_2 (ps) $S_1 \rightarrow {}^*S_0$	τ_3 (ps) $^*S_0 \rightarrow S_0$	τ_4 (ps) $^*S_0 \rightarrow$ *cis*-S_0	τ_5 (min)‡ *cis*-$S_0 \rightarrow$ *trans*- S_0
Nap-azo-ph (**1**)	328	421	0.05 ± 0.07	0.64 ± 0.20	2.9 ± 0.3	22 ± 3	n/o	280
Nap-azo-phOH (**2**)	357	403	0.04 ± 0.05	1.19 ± 0.20	3.0 ± 0.5	32 ± 4	n/o	12
Nap-azo-phOMe (**3**)	357	420	0.05 ± 0.03	1.38 ± 0.14	3.7 ± 0.7	25 ± 1	n/o	24
Nap-azo-phNMe$_2$ (**4**)	421	n/a	n/a	0.70 ± 0.04	3.4 ± 0.9	16. ± 1	38 ± 5	8

n/o indicates that the process is not observed on our TAS measurements due to the spectral observation window available in our measurements. Based on the residual component (i.e. τ_5 inf, we infer that the process does occur, but that we are not able to observe it in TAS).

‡ Based on steady-state reversion kinetics shown in Figure S1.

Table 2. Structural parameters for the fully optimized trans- and cis- isomer and a transition state between them, as well as the TDDFT S_1 of azo **1** and azo **4**. B3LYP/6-311G(d,p)/PCM(ACN).

optimized structure		N-N (Å)	∠^{nap}CNN (°)	∠^{ph}CNN (°)	∠CNNC (°)
trans-	**1**	1.26	115.3	115.3	180.0
cis-		1.26	124.4	125.8	11.8
TS		1.22	117.8	180.0	(104.6)
S_1		1.25	130.0	130.7	180.0
trans-	**4**	1.26	114.9	116.3	180.0
cis-		1.25	124.3	125.8	10.2
TS		1.23	180.0	119.1	(24.6)
S_1		1.25	130.8	129.7	180.0

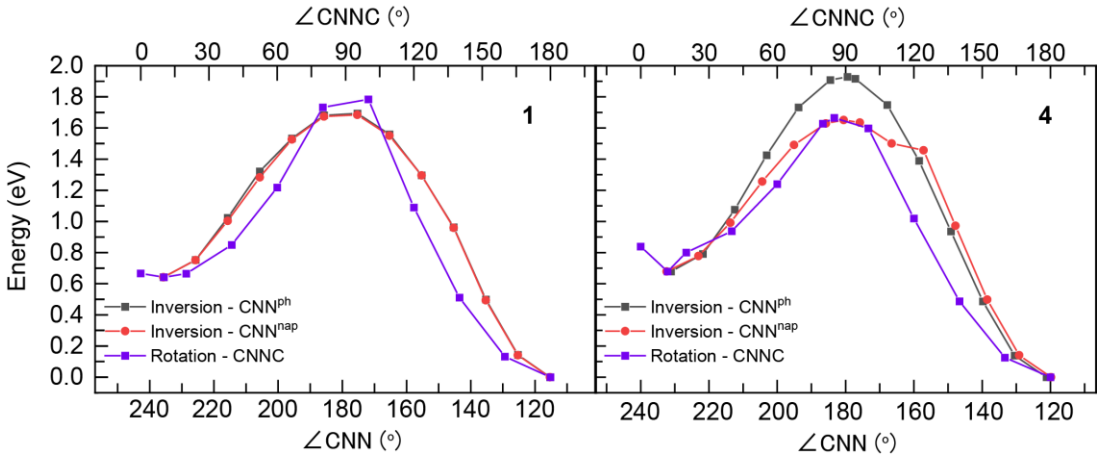

Figure 5. trans(∠CNNC 180°)-cis-(∠CNNC 0°)-isomerization barriers on the ground state (S_0) surfaces of azo **1** and **4**. B3LYP/6-311G(d,p)/PCM(ACN) relaxed scans, where the barrier energy matches the fully relaxed TS (Table 2) geometries.

irradiation is stopped, *cis* → *trans* thermal reversion is observed (Figure S1a,b) the lifetime of which varies substantially depending on the derivative. The unsubstituted derivative (**1**) has a reversion lifetime of ~280 min, while the substituted derivatives (**2** – **4**) reveal shorter reversion times of 12 min (**2**), 24 min (**3**) and 8 min (**4**). A plot of the log of the reversion lifetime against the Hammett parameter of the substituent show a linear trend of decreasing reversion lifetime with increasing electron donating strength (Figure 4).[46] These results demonstrate that electronic effects play a significant role in the isomerization of these naphthalene-based azo dyes.

Ground state *cis–trans reversion* isomerization in other azo dyes can proceed through either an inversion or a rotation of the azo bond depending on the reaction conditions. The inversion on the ground-state surface, on either the naphthalene or the phenyl side of the azo, and the rotation of the azo bond show near identical barriers in azo **1** (Figure 5), whereas the phenyl inversion barrier in azo **4** has a higher barrier than that of the naphthalene inversion and the rotation. Interestingly, while the *trans*- and *cis*-isomers in both azo **1** and **4** have similar structure, the relaxed transition states (as confirmed by one imaginary frequency) have quite different geometries (Table 2). In the transition state of azo **1**, the phenyl ring is found to rotate towards the plane that is perpendicular to naphthalene and the connected CNN angle is bent from 115° to 180° (Figure S22-26). In azo **4**, the phenyl ring stays unchanged, however, the CNN bond on the naphthalene side is bent to 180° and the naphthalene is rotated to become perpendicular to the phenyl ring (Figure S33-36). The optimized transitions states match geometrically and energetically with the phenyl and naphthalene inversions calculated through scanning the respective angles (Figure 5) for azo **1** and **4**, respectively. This ground state inversion pathway is consistent with the ground state thermal isomerization seen in many azos.[15,47]

Time evolution of the excited states. To further understand the differences observed in steady-state absorption and emission spectra of azo **1** – **4**, transient absorption (TA) spectroscopy was performed on azo **1** – **4** in degassed acetonitrile prepared by freeze-pump-thaw to mtorr pressures.

Figure 6 (left column) shows the TA spectral evolution over ~5 ns for **1** – **4**. The induced absorptions in the transient signals of azo **1** – **3** (Figure 6) share similar broad induced absorption features between 390 nm and 625 nm. Broad induced absorption peaks centered at ~425 nm and ~555 nm were

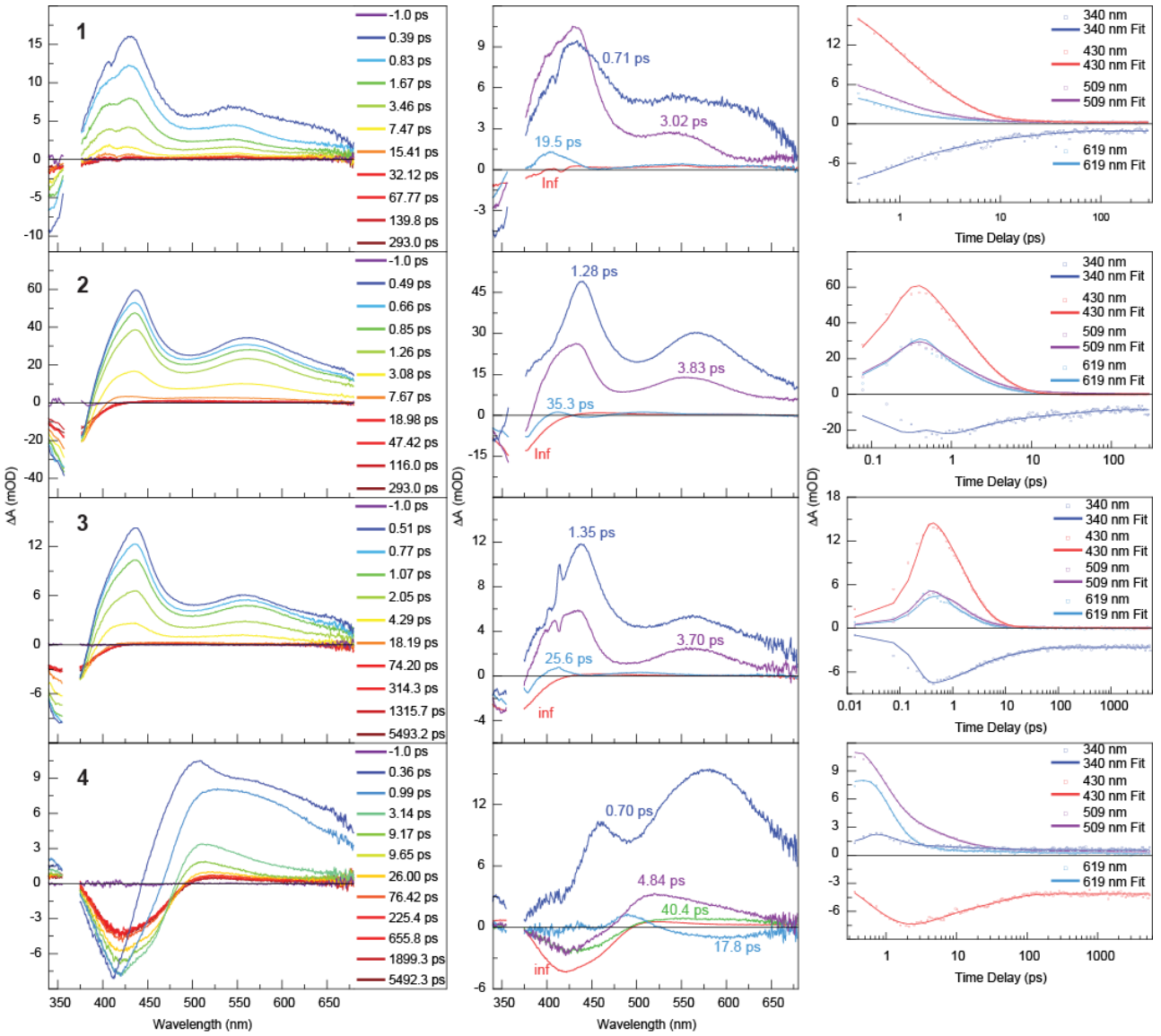

Figure 6. (left) Transient absorption (TA) representative spectra of azo **1 – 4** in acetonitrile (λ_{ex} = 370 nm). Samples were prepared under a nitrogen environment in a 2-mm quartz high-vacuum cuvette. Concentrations are: **1**, 25 μM; **2**, 18 μM; **3**, 16 μM; **4**, 28 μM. (middle) Decay-associated difference spectra (DADS) from global analysis fitting of azo **1 – 4** with associated lifetimes next to each spectrum for the individual run shown. Averages of at least three different runs are reported with standard deviations in Table 1. (right) Single-wavelength fits (solid lines) of the data (dotted lines) based on the proposed model obtained from GLA.

observed for azo **1 – 3** at the shortest times resolvable on our instrumentation (~0.4 ps representative spectrum on Figure 6 left column). These peaks are indicative of a hot S_1 state that undergoes rapid vibrational cooling (~1ps) to the S_1 state (with a ~3 ps lifetime). Both the representative spectra, as well as the two DADS associated with these processes, show a blue-shift of the spectra/DADS over the first few ps that are indicative of a vibrational cooling process. Even though excitation occurs into the S_3 and S_2 states, the deactivation of those two states is too rapid for our system to resolve and we begin our observation in the hot S_1 state. Of note, the broad hot S_1 peak shifts slightly to the red and becomes more intense as the electron donating nature of the substituent is increased from **1** (no substituent) to **3** (-OMe substituted) and **2** (-OH substituted). Weak residuals were observed at the end of our 5-ns TAS window with intensities less than 1% of the original signal. The residual is likely due to isomerized *cis*-azo dye (**1 – 3**) that does not convert back to the *trans*-isomer (Figure S32) in the 5-ns window and is too weak to be observed in the nanosecond transient absorption experiment.

The spectral evolution of the TA spectra for azo dye **4** is different than those of **1 – 3**. A broad induced absorption between 500 nm and 625 nm convolved with a bleach between 375 nm and 500 nm was observed (Figure 6) upon initial excitation. The peak indicative of the hot S_1 is much broader in **4**. There appears to be two features within the broad 500-625 nm induced absorption (at 460 nm and 580 nm) that decay concomitantly leaving an induced absorption at ~525 nm. This broad absorption at 525 nm decays to the baseline leaving a small peak at ~510 nm, which remains at the end of the 5-ns window

for ultrafast TA. Meanwhile the ground-state bleach at 375-500 nm only decayed by ~50% by the end of the 5-ns window. Our attempts to accurately measure the nanosecond component was not successful due to the limited signal to noise in the spectral region accessible in our nanosecond TAS setup (460 nm – 900 nm).

Global lifetime analysis (GLA) fitting of the TAS data was carried out to extract the lifetimes and corresponding associated difference spectra (DADS) (Figure 6 middle column) that contribute to the excited state evolution of **1 – 4**. The lifetimes obtained from GLA were then used to construct single-wavelength traces at various wavelengths across the spectral region that were compared to the TAS data extracted at those wavelengths (Figure 6 right column). GLA was performed using three to six lifetimes and the best fit to the data was determined and set as the model. Detailed description of the fitting, as well as residuals comparing the data to the fit, and single wavelength fits for each moiety are show in the Supporting Information (Figures S10-S17).

GLA fitting produced DADS with associated lifetimes shown in Figure 6 (middle column) and summarized Table 1. GLA produces an "infinite" component for each azo, representing the residual signal that does not decay on our 5.5 ns time window and therefore cannot be assigned a lifetime. The residual component likely stems from the formation of the *cis*-isomer that does not convert back to the *trans*-isomer over the 5-ns window as shown by comparison of the final representative spectrum with the *cis*/*trans* difference spectrum obtained from the steady-state absorption spectra in Figure 7 (and Figure S19). GLA produces three additional lifetimes in azo **1 – 3**. The first component fits to lifetimes of 0.6 – 1.38 ps for azo **1 – 3**, while the second component has slightly longer lifetimes of 2.9 – 3.7 ps and the third component has a lifetime of 20 – 30 ps. For **4**, GLA produces four components of 0.7(4) ps, 3.4(9) ps, 16(1) ps and 38(5) ps.

The shortest-lifetime DADS component (0.71 ps) of azo **1** shows a broad spectrum in the range between 450 nm to 700 nm, with peaks centered at 460 nm and 580 nm. The shortest-lifetime DADS components of azo **2** and **3** (1.28 ps, and 1.35 ps) show more well resolved peaks (also centered around 460 nm and 580 nm) on a broad positive-going signal to the red of 375 nm. The second DADS components of azo **1 – 3** (~3 ps) share similar features to that of the shortest DADS including positive-going peaks that are slightly blue-shifted from those observed the shortest DADS. The third DADS (20 – 30 ps) shows a weak positive going peak centered ~400 nm. The "infinite" component for each moiety resembles that that of the cis/trans difference spectrum (*vide supra*, Figure 7 and Figure S32)

In the case of azo **4**, the 0.7-ps shortest-lifetime DADS component has broad positive-going features centered at 460

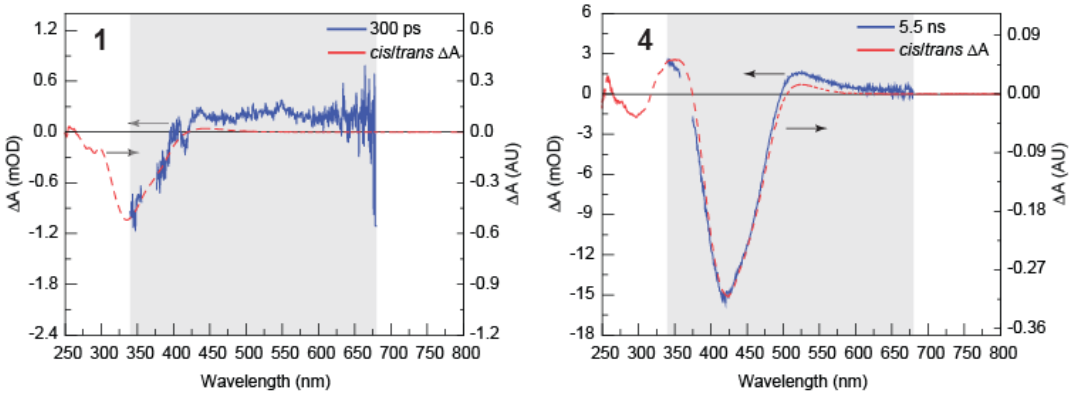

Figure 7. Comparison of the *cis*/*trans* difference spectra obtained by steady-state spectroscopy (red dotted line) with the "residual" representative spectra observed in TAS (blue solid line) for **1** (left) and **4** (right). The grey shaded area represents the spectral window available on the TAS measurement.

Scheme 3. Schematic Diagram of the Relaxation of azo **1** – **3** and **4** after excitation at 370 nm in CH_3CN.

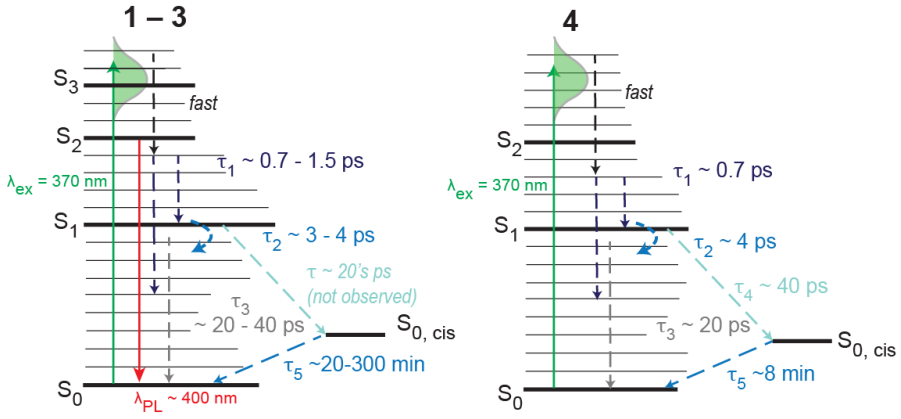

nm and 580 nm that extend across most of the spectral window, red of 400 nm that looks to be convolved with a negative-going feature on the blue edge of the spectral window. The second DADS component (4.84 ps) of azo **4** shows a positive-going peak centering at 508 nm and the negative-going signal in the range 400 – 475 nm. The third DADS component (17.8 ps) has a positive-going peak at 475 nm and a negative-going peak at ~600 nm. The fourth DADS component (40.4 ps) has a similar shape as the second component but with lower intensity on the positive-going component. As is the case for **1 – 3**, the "infinite" component of **4** matches very closely to the cis/trans difference spectrum obtained from steady-state absorptions spectra.

The lifetimes determined by GLA fitting, when represented as single wavelength decay traces represent the data well across the entire spectral window for each of the azo moieties **1 – 4**, Figure 6 (right), lending support for each of the proposed models.

It has been widely accepted that in azobenzene the S_2 excited state has an extremely short lifetime of 0.1 ps, followed by rapid internal conversion to the S_1 excited state.[41] The S_1 excited state is reported to have a lifetime of 0.5 ps. The conical intersection between the S_1 and S_0 state can lead to isomerization of the azo moiety to a *cis*-configuration or a vibrationally excited ground state (S_0). This "hot" S_0 state is reported to have a "long" vibrational cooling process with lifetimes of around 2 - 15 ps depending on solvent and relaxation mechanisms (either rotation or inversion).[48]

The overall picture for the excited-state dynamics of the naphthalene-based azo **1** – **4** (Figure 7 and Scheme 3) can be assigned to the same model as azobenzne. However, our instrument response function does not allow us to resolve the sub-ps lifetime associated with the S_2 decay, which seems to be more rapid in **1** – **4** compared to azobenzene. As a point of comparison, we have collected TAS data on azobenzene and show direct comparison of our azobenzene data to our results for **1** – **4** (Supporting Information Figure S18). Namely, for azobenzene, our instrument is able to capture and resolve a glimpse of the rapid $S_2 \rightarrow S_1$ process that occurs on a ~0.2 ps time scale and is observed as a peak at 465 nm (the S_2) that disappears rapidly into the broad peak at 400 nm (the S_1). We are able to reproduce decay dynamics that have been reported previously for such systems on short times scales.[21–23]

When **1**, **2**, and **3** are excited at 370 nm, an initial $S_0 \rightarrow S_2$ ($\pi\pi^*$) and $S_0 \rightarrow S_3$ ($\pi\pi^*$) excitation occurs (Table S1, S3, and S5). The S_3 excited state should decay within the instrument response through S_3 ($\pi\pi^*$) $\rightarrow S_2 \rightarrow {}^*S_1$ internal conversion resulting in a hot S_1 state, which can then decay through radiative emission or a non-radiative pathway. We do not observe a signal corresponding to the S_2 state meaning that this state in the naphthalene-based azo dyes decays more rapidly than the azobenzene S_2 state (which we are able to resolve, Figure S18). The non-radiative pathway we observe therefore begins with a hot S_1 state (peak at ~425 nm and ~555 nm) that cools to the S_1 state and is resolved as the most rapid lifetime we observe τ_1 =~0.7-1.5 ps. The relaxation of the S_1 to a hot the ground state takes τ_2 ~ 3-4 ps. A lifetime of ~10 ps has previously been assigned to vibrational cooling of a hot S_0 state in azobenzenes.[48,49] The features associated with this vibrational cooling process are typically blue-shifted and convolved with the bleach features in the TAS spectra. The third lifetime (τ_3) we observe (20-30 ps) is consistent with both the expected lifetime and spectral features of vibrational cooling and we have therefore assigned that lifetime to the vibrational cooling process. Additionally, photoisomerization of the *trans* to *cis* configuration contributes to the photophysical decay pathway. Photoisomerization and thermal reversion measurements (Figure S1, for azos **1** – **4**) of these species show that **1**, **2** and **3** convert to a *cis* configuration upon 420 nm illumination. In each species, when illumination is ended, the *trans* configuration is recovered over the course of minutes (**2**) to hours (**1** and **3**). Indeed, the residual component in the TAS representative spectra and DADS (τ_5) are likely the *cis* configuration of each moiety (Figure S19). Therefore, we might expect to also observe a lifetime associated with the *trans* to *cis* isomerization process via internal conversion from the S_1. We do observe an additional lifetime in **4** (τ_4) that is missing in **1 – 3**. We posit that this lifetime represents the isomerization process. The spectral features of **1** – **3** associated with the *trans* to *cis* isomerization do not fall well into the spectral window of our TAS instrumentation (depicted as the grey region in Figure 7 as comparison). We therefore are likely missing a ~30-40 ps lifetime in our data that would represent the isomerization process.

The TAS spectra, DADS, and excited-state dynamics of azo **4** deviate somewhat from what is observed for **1 – 3** and azobenzene. One advantage of **4** is that the absorption spectrum is better overlapped with our spectral window in TAS, which allows us more insight to the dynamics. Another major difference is that no emission is observed from **4**. The shortest-lifetime component DADS obtained from **4** has a broader spectrum compared to the shortest-lifetime DADS of **1 – 3** and has a slightly shorter lifetime of τ_1 = 0.7 ps, indicating more rapid vibrational cooling to the S_1 state. The S_1 state (τ_2 = 4.84 ps) is then resolved and leads to population of the hot S_0 and some initial recovery of S_0 (indicated by the negative going peak at 425 nm in the DADS). This hot S_0 state undergoes vibrational cooling to the *trans*-ground state (τ_3 = 17.8 ps). Alternatively, the conical intersection between S_1 and S_0 that allows for isomerization to the *cis*-configuration, is red-shifted in azo **4** and thus its relaxation to the *cis*-ground state can be resolved (τ_4 = 40.4 ps).

Excited-state potential energy surfaces of azos 1 – 4. As part of our computational characterization of azos **1 – 3**, we computed potential energy curves (PEC) of the singlet and triplet excited state manifold as well as spin orbit coupling constants. The flat nature of excited state surfaces might lead to rapid isomerization or geometric reorganization in longer-lived excited states. To explore this possibility, additional quantum mechanics calculations were performed to better understand the excited state energetics of the *trans–cis* interconversion. Azo **1** was selected as the

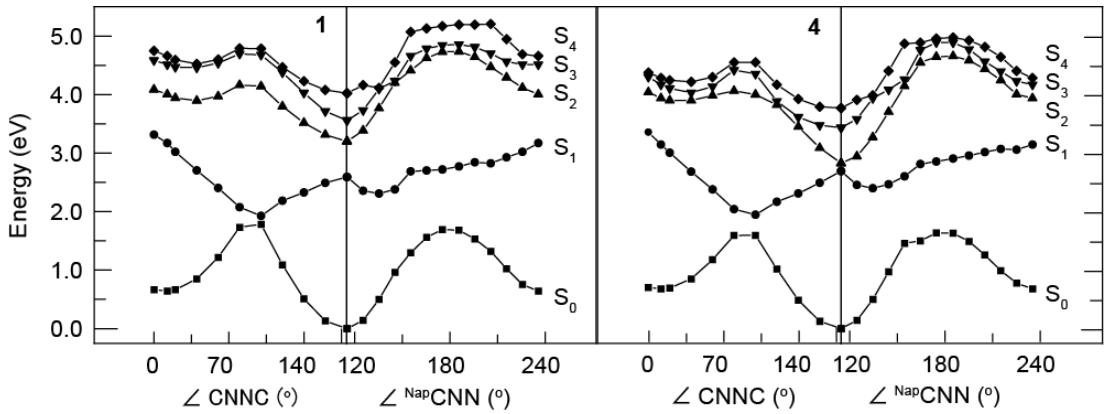

Figure 8. Singlet PECs below 5 eV in energy along the torsional (∠CNNC) and inversion (∠^{Nap}CNN) S_0 trans-cis isomerization. The excited state (TDDFT) surfaces above each shown point are plotted and like excited states are connected with lines. B3LYP/6-311G(d,p)/PCM(ACN).

representative of azo **1** – **3** and traces of its potential energy surfaces (or potential energy curves, PECs) were compared to those of azo **4**.

Trans to *cis* conversion can occur though rotation of the CNNC azo bond or via CNN inversion on either the phenyl or naphthalene side. While the rotation pathway does not dominate measured ground-state isomerization, it has been suggested that photoisomerization on the excited-state surfaces may proceed through this pathway. Thus we calculated the vertical singlet excitations above both the lowest energy inversion on the naphthalene side for azo **1** and **4** and the rotation PECs (Figure 8). These surfaces show similar shapes and features as many different methods that have been used to explore the photochemistry of azobenzenes.[17–20,50] Except for S_1 surfaces, the minimum energy point of all the singlet excited state PECs fall at similar positions near the initial Franck-Condon (optimized ground state) geometry for azo **1** and **4**. Similar to the ground state surfaces, the highest energy of each S_2 and higher PEC is close to the mid-point between the *cis*-*trans* isomerization of each pathway. In contrast, the S_1 PECs of both dyes, have a minimum in the middle of torsional rotation with a CNNC angle close to 100° and near the *cis*-isomer along the inversion axis, with a ~ 130° CNN angle. Thus, the internal conversion conical intersection between S_1 and S_0 in both azo **1** and **4** generate high energy ground state structures near the transition state between the *trans* and *cis* isomers allowing a population of each to be formed.

Recently, exploration of the nonadiabatic dynamics of the populations of *cis* and *trans* generated by the S_1 to S_0 internal conversion have quantified that about 15% of azobenzene photoexcitation results in population of the *cis*-isomer.[50–54] We would expect similar populations of ground state *cis*- and *trans*-isomer for azo dyes **1** – **4** as the underlying quantum mechanical potential energy surfaces are so similar to those used to generate the molecular dynamics potential used in those studies. In addition, although triplet states are less common in azo dyes,[55,56] prior work has shown that the large spin orbit coupling of S_0 and T_1 might enable triplet facilitation of *trans*–*cis* photoisomerization of azo molecules.[47] Our computational work is presented in the supporting information and determined that triplets do not play a major role in these systems.

Conclusions

In summary, we present a systematic, photophysical property study of several naphthalene derived azo species. By varying substituents on the 4-phenyl position, we increase the excited-state lifetimes for the most electron donating substituents (**4**, –NMe_2) while shortening the *cis* → *trans* reversion lifetimes.

For azo **1** – **3**, the initial S_2/S_3 excitation relaxes to S_1 state rapidly (during our instrument response time). The resulting hot S_1 cools to the S_1 (~1 ps) state and undergoes further internal conversion to the hot S_0 ground state (~3 ps). From the hot S_0, relaxation to the ground *trans*-isomer (20-40 ps) occurs. Internal conversion from the S_1 to *cis*-ground state (on S_0) occurs, however we are unable to resolve this process experimentally in our TAS studies. Due to experimental limitations of the TAS detection window we hypothesize that we miss a ~20 ps lifetime that represents this *trans* → *cis* isomerization process. Quantum mechanics suggests that the fast $S_1 \rightarrow S_0$ conversion is facilitated through rotation of the CNNC dihedral angle, with vibrational and geometric cooling on the S_0 surface. The high electron donation in the dimethyl amino substituted azo **4**, elongates the excited-state lifetimes in this moiety. In azo **4**, the hot S_1 state formed via rapid internal conversion from an S_2 excitation has a lifetime of ~1 ps. Internal conversion to S_0 occurs with a lifetime of 4 ps. Upon internal conversion, we observe thermal relaxation to the *trans*-isomer (20 ps). Branching in the S_1 leads to an internal converstion at the conical intersection that results in isomerization to form the *cis*-isomer (40 ps).

Dyes that access the *cis* isomer thermally revert the *trans* configuration. Lifetimes measured for this process vary from minutes (**2**, **3**, **4**) to hours (**1**). The lifetime of the *cis* configuration decreases non-linearly with the increasing value of the Hammett parameter with the most electron-donating substituent (-NMe_2) resulting in the shortest-lived *cis*-isomer.

Author Contributions

Tao Huang: Investigation (equal), Formal analysis, Writing – original draft; Shea Martin: Investigation (equal), Formal analysis; Robert Hamburger: Investigation (equal), Validation, Formal analysis; Craig Pointer: Investigation (equal) ; Lisa Fredin: Conceptualization, Supervision, Writing – review & editing; Elizabeth Young: Conceptualization, Supervision, Writing – original draft.

Conflicts of interest

There are no conflicts to declare.

Acknowledgements

The authors thank the NSF Major Research Instrumentation program (CHE-1428633) for funding that established the laser facility. This work made use of the Lehigh University NMR Facility. The Bruker Neo 500 MHz NMR was acquired through NSF-MRI-1725883, with additional support from Lehigh University. Portions of this research were conducted with research computing resources provided by Lehigh University and the TG-CHE190011 allocation from Extreme Science and Engineering Discovery Environment (XSEDE), which is supported by National Science Foundation grant number ACI-1548562. Financial support for this research comes from Lehigh University.

References

1 A. Bafana, S. S. Devi and T. Chakrabarti, *Environ. Rev.*, 2011, **19**, 350–370.
2 C. Cobbold, *Ambix*, 2019, **66**, 23–50.
3 S. H. Ramugade, U. S. Warde and N. Sekar, *Dye. Pigment.*, 2019, **170**, 107626.
4 V. R. Mishra, C. W. Ghanavatkar and N. Sekar, *J. Lumin.*, 2019, **215**, 116689.
5 S. Suwanprasop, T. Nhujak, S. Roengsumran and A. Petsom, *Ind. Eng. Chem. Res.*, 2004, **42**, 4973–4978.
6 D. Bandara and S. Burdette, *Chem. Soc. Rev.*, 2012, **41**, 1809–1825.
7 Y. Ali, S. A. Hamid and U. Rashid, *Mini-Reviews Med. Chem.*, 2018, **18**, 1548–1558.
8 L. Zhang and J. M. Cole, *ACS Appl. Mater. Interfaces*, 2014, **6**, 3742–3749.
9 P. S. Addy, Y. Zheng, J. S. Italia and A. Chatterjee, *ChemBioChem*, 2019, **20**, 1659–1663.
10 D. Das and A. R. Choudhury, *CrystEngComm*, 2019, **21**, 2373–2380.
11 A. N. Oldacre and E. R. Young, *RSC Adv.*, 2020, 14804–14811.
12 A. N. Oldacre, C. A. Pointer, S. M. Martin, A. Kemmerer and E. R. Young, *Chem. Commun.*, 2019, **55**, 5875–5877.
13 J. C. Lennox, D. A. Kurtz, T. Huang and J. L. Dempsey, *ACS Energy Lett.*, 2017, **2**, 1246–1256.
14 T. Fujino and T. Tahara, *J. Phys. Chem. A*, 2000, **104**, 4203–4210.
15 H. M. D. Bandara and S. C. Burdette, *Chem. Soc. Rev.*, 2012, **41**, 1809–1825.
16 C. G. Morgante and W. S. Struve, *Chem. Phys. Lett.*, 1979, **68**, 267–271.
17 I. K. Lednev, T.-Q. Ye, P. Matousek, M. Towrie, P. Foggi, F. V. R. Neuwahl, S. Umapathy, R. E. Hester and J. N. Moore, *Chem. Phys. Lett.*, 1998, **290**, 68–74.
18 I. K. Lednev, T.-Q. Ye, R. E. Hester and J. N. Moore, *J. Phys. Chem.*, 1996, **100**, 13338–133341.
19 F. Aleotti, L. Soprani, A. Nenov, R. Berardi, A. Arcioni, C. Zannoni and M. Garavelli, *J. Chem. Theory Comput.*, 2019, **15**, 6813–6823.
20 M. Quick, A. L. Dobryakov, M. Gerecke, C. Richter, F. Berndt, I. N. Ioffe, A. A. Granovsky, R. Mahrwald, N. P. Ernsting and S. A. Kovalenko, *J. Phys. Chem. B*, 2014, **118**, 8756–8771.
21 C. Slavov, C. Yang, L. Schweighauser, C. Boumrifak, A. Dreuw, H. A. Wegner and J. Wachtveitl, *Phys. Chem. Chem. Phys.*, 2016, **18**, 14795–14804.
22 C. J. Otolski, A. Mohan Raj, V. Ramamurthy and C. G. Elles, *J. Phys. Chem. Lett.*, 2019, **10**, 121–127.
23 C. J. Otolski, A. M. Raj, V. Ramamurthy and C. G. Elles, *Chem. Sci.*, 2020, **11**, 9513–9523.
24 J. Azuma, N. Tamai, A. Shishido and T. Ikeda, *Chem. Phys. Lett.*, 1998, **288**, 77–82.
25 Y. Hirose, H. Yui and T. Sawada, *J. Phys. Chem. A*, 2002, **106**, 3067–3071.
26 B. Maerz, S. Wiedbrauk, S. Oesterling, E. Samoylova, A. Nenov, P. Mayer, R. De Vivie-Riedle, W. Zinth and H. Dube, *Chem. - A Eur. J.*, 2014, **20**, 13984–13992.
27 J. R. Lakowicz, *Principles of Fluorescence Spectroscopy*, Springer US, Boston, MA, 1999.
28 R. Ditchfield, W. J. Hehre and J. A. Pople, *J. Chem. Phys.*, 2004, **54**, 724–728.
29 M. M. Francl, W. J. Pietro, W. J. Hehre, J. S. Binkley, M. S. Gordon, D. J. DeFrees and J. A. Pople, *J. Chem. Phys.*, 1982, **77**, 3654–3665.
30 W. J. Hehre, K. Ditchfield and J. A. Pople, *J. Chem. Phys.*, 1972, **56**, 2257–2261.
31 P. C. Hariharan and J. A. Pople, *Theor. Chim. Acta*, 1973, **28**, 213–222.
32 A. D. Becke, *J. Chem. Phys.*, 1993, **98**, 5648–5652.
33 C. Lee, W. Yang and R. G. Parr, *Phys. Rev. B*, 1988, **37**, 785–789.
34 S. H. Vosko, L. Wilk and M. Nusair, *Can. J. Phys.*, 1980, **58**, 1200–1211.
35 P. J. Stephens, F. J. Devlin, C. F. Chabalowski and M. J. Frisch, *J. Phys. Chem.*, 1994, **98**, 11623–11627.

36 F. Weigend, M. Häser, H. Patzelt and R. Ahlrichs, *Chem. Phys. Lett.*, 1998, **294**, 143–152.
37 J. Tomasi, B. Mennucci and R. Cammi, *Chem. Rev.*, 2005, **105**, 2999–3093.
38 M. J. Frisch, G. W. Trucks, H. B. Schlegel, G. E. Scuseria, M. A. Robb, J. R. Cheeseman, G. Scalmani, V. Barone, G. A. Petersson, H. Nakatsuji, X. Li, M. Caricato, A. V Marenich, J. Bloino, B. G. Janesko, R. Gomperts, B. Mennucci, H. P. Hratchian, J. V Ortiz, A. F. Izmaylov, J. L. Sonnenberg, D. Williams-Young, F. Ding, F. Lipparini, F. Egidi, J. Goings, B. Peng, A. Petrone, T. Henderson, D. Ranasinghe, V. G. Zakrzewski, J. Gao, N. Rega, G. Zheng, W. Liang, M. Hada, M. Ehara, K. Toyota, R. Fukuda, J. Hasegawa, M. Ishida, T. Nakajima, Y. Honda, O. Kitao, H. Nakai, T. Vreven, K. Throssell, J. A. Montgomery Jr., J. E. Peralta, F. Ogliaro, M. J. Bearpark, J. J. Heyd, E. N. Brothers, K. N. Kudin, V. N. Staroverov, T. A. Keith, R. Kobayashi, J. Normand, K. Raghavachari, A. P. Rendell, J. C. Burant, S. S. Iyengar, J. Tomasi, M. Cossi, J. M. Millam, M. Klene, C. Adamo, R. Cammi, J. W. Ochterski, R. L. Martin, K. Morokuma, O. Farkas, J. B. Foresman and D. J. Fox, 2016.
39 G.-Q. Li, H. Gao, C. Keene, M. Devonas, D. H. Ess and L. Kürti, *J. Am. Chem. Soc.*, 2013, **135**, 7414–7417.
40 K. Wojciechowski, *Dye. Pigment.*, 1988, **9**, 401–417.
41 T. Fujino, S. Y. Arzhantsev and T. Tahara, *J. Phys. Chem. A*, 2001, **105**, 8123–8129.
42 A. P. Demchenko, V. I. Tomin and P.-T. Chou, *Chem. Rev.*, 2017, **117**, 13353–13381.
43 H. Rau, *J. Photochem.*, 1984, **26**, 221–225.
44 A. Nenov, R. Borrego-Varillas, A. Oriana, L. Ganzer, F. Segatta, I. Conti, J. Segarra-Marti, J. Omachi, M. Dapor, S. Taioli, C. Manzoni, S. Mukamel, G. Cerullo and M. Garavelli, *J. Phys. Chem. Lett.*, 2018, **9**, 1534–1541.
45 I. Conti, M. Garavelli and G. Orlandi, *J. Am. Chem. Soc.*, 2008, **130**, 5216–5230.
46 A. R. Allen, J. F. Poon, R. C. McAtee, N. B. Watson, D. A. Pratt and C. R. J. Stephenson, *ACS Catal.*, 2022, **12**, 8511–8526.
47 A. Cembran, F. Bernardi, M. Garavelli, L. Gagliardi and G. Orlandi, *J. Am. Chem. Soc.*, 2004, **126**, 3234–3243.
48 C.-W. Chang, Y.-C. Lu, T.-T. Wang and E. W.-G. Diau, *J. Am. Chem. Soc.*, 2004, **126**, 10109–10118.
49 L. Wang, W. Xu, C. Yi and X. Wang, *J. Mol. Graph. Model.*, 2009, **27**, 792–796.
50 J. K. Yu, C. Bannwarth, R. Liang, E. G. Hohenstein and T. J. Martínez, *J. Am. Chem. Soc.*, 2020, **142**, 20680–20690.
51 A.-H. Gao, B. Li, P.-Y. Zhang and K.-L. Han, *J. Chem. Phys.*, 2012, **137**, 204305.
52 M. Pederzoli, J. Pittner, M. Barbatti and H. Lischka, *J. Phys. Chem. A*, 2011, **115**, 11136–11143.
53 R. Liang, *J. Chem. Theory Comput.*, 2021, **17**, 3019–3030.
54 L. Yu, C. Xu, Y. Lei, C. Zhu and Z. Wen, *Phys. Chem. Chem. Phys.*, 2014, **16**, 25883–25895.
55 H. Goerner, H. Gruen and D. Schulte-Frohlinde, *J. Phys. Chem.*, 1980, **84**, 3031–3039.
56 W. Adam, G. Fragale, D. Klapstein, W. M. Nau and J. Wirz, *J. Am. Chem. Soc.*, 1995, **117**, 12578–12592.